PCCP

Efficient Sampling of Molecular Orientations for Cu(II)-based DEER on protein labels

SCHOLARONE™
Manuscripts

ARTICLE

Efficient Sampling of Molecular Orientations for Cu(II)-based DEER on protein labels

Zikri Hasanbasri,[a] Nicholas A. Moriglioni,[a] and Sunil Saxena *[a]

Combining rigid Cu(II) labels and pulsed-EPR techniques enables distance constraint measurements that are incisive probes of protein structure and dynamics. However, the labels can lead to a dipolar signal that is biased by the relative orientations of the two spins, which is typically unknown a *priori* in a bilabeled protein. This effect, dubbed orientational selectivity, becomes a bottleneck in measuring distances. This phenomenon also applies to other pulsed-EPR techniques that probe electron-nucleus interactions. In this work, we aim to dissect orientational selectivity by generating an in-silico sample of Cu(II)-labeled proteins to evaluate pulse excitation in the context of Double Electron-Electron Resonance (DEER) at Q-band frequencies. This approach enables direct observation of the contribution of each protein orientation to the dipolar signal, which provides direct insights into optimizing acquisition schemes to mitigate orientational effects. Furthermore, we incorporate the excitation profile of realistic pulses to identify the excited spins. With this method, we show that rectangular pulses, despite their imperfect inversion capability, can sample similar spin orientations as other sophisticated pulses with the same bandwidth. Additionally, we reveal that the efficiency of exciting spin-pairs in DEER depends on the frequency offset of two pulses used in the experiment and the relative orientation of the two spins. Therefore, we systematically examine the frequency offset of the two pulses used in this double resonance experiment to determine the optimal frequency offset for optimal distance measurements. This procedure leads to a protocol where two measurements are sufficient to acquire an orientational-independent DEER at Q-band. Notably, this procedure is feasible with any commercial pulsed-EPR spectrometer. Furthermore, we experimentally validate the computational results using DEER experiments on two different proteins. Finally, we show that increasing the amplitude of the rectangular pulse can increase the efficiency of DEER experiments by almost threefold. Overall, this work provides an attractive new approach for analyzing pulsed-EPR spectroscopy to obtain microscopic nuances that cannot be easily discerned from analytical or numerical calculations.

Introduction

Cu(II)-based spin labels[1] are a powerful class of labels for EPR measurements of protein structure and dynamics. Specifically, Continuous Wave (CW) EPR experiments on Cu(II) labeled biomolecules can measure site-specific dynamics when the Cu(II) label is attached to a selected site on a protein[2,3]. Additionally, when two or more sites are labeled, distance measurements can be obtained between these sites using pulsed dipolar spectroscopy[4–10]. While these experiments are routinely conducted using many other spin labels [11–13], Cu(II) is unique due to its labeling strategy. For protein labeling, a chelated Cu(II) coordinates to two strategically engineered histidine residues, known as a dHis motif[14]. Because two residues anchor Cu(II), the conformational space of Cu(II) is highly correlated with the structure, flexibility, and motion of the protein backbone[15]. As a result, room temperature CW-EPR

experiments on dHis-Cu(II) are incisive probes of backbone dynamics and are sensitive to time scales as small as 50 ps[2,3]. Furthermore, distance measurements between two dHis-Cu(II) sites are up to five times narrower than commonly used nitroxide labels[14]. Such narrow distributions enable the resolution of multiple conformations that otherwise would be indistinguishable using other labels[16]. The measurements can, in principle, obtain distances up to 9 nm when the system is deuterated[17]. In addition to distances, the rigidity of the label enables the straightforward measurement of the relative orientation between two sites[18], and the trilateration of a native binding site with a minimal number of distance constraints[19]. The dHis-Cu(II) labeling can also be paired with other labels to allow measurements at nanomolar concentrations[20,21]. Such orthogonal labeling schemes have also provided a new pathway to measure equilibrium properties at concentrations lower than Isothermal Titration Calorimetry[22]. Cu(II)-based labels have also been developed for DNA. For example, the dipicolylamine can be incorporated into DNA strands in a nucleotide-independent manner, allowing distance measurements that directly assay the backbone conformations of the DNA[23,24] to measure DNA conformational changes[25]. Another Cu(II)-based DNA label uses a G-quadruplex motif to attach Cu(II) at the ends of the DNA strand[26–28].

[a.] Department of Chemistry, University of Pittsburgh, PA 15260, USA.
* To whom correspondence should be addressed: ORCID: 0000-0001-9098-6114, Phone (412) 624-8680. Email: sksaxena@pitt.edu

Despite the success of Cu(II)-based labels, these labels suffer from the broad EPR spectral width. The Cu(II) EPR spectrum is ca. 5 GHz at Q-band frequencies, which is ~18 times broader than nitroxide labels. This broad spectrum leads to two problems. First, rectangular pulses with narrow bandwidth in commercial spectrometers cannot efficiently excite Cu(II) labels. As a result, the probability of exciting the intramolecular signal is low compared to other spin labels, reducing the sensitivity. This loss is somewhat compensated by operation at ca. 20 K, leading to higher spin polarization[29,30]. Such temperatures are often impractical with other labels. The recent developments of Ultra-Wideband arbitrary wave generators[31] and loop-gap resonators[32] further alleviate the sensitivity problem. These approaches enable pulses with large excitation bandwidths to excite larger portions of the Cu(II) spectrum. In addition, sample deuteration reduces dephasing during spin evolution[17]. As a result, the deuteration increases the relaxation time of Cu(II), increasing the echo signal.

The second concern is that the low excitation bandwidth of pulses can lead to the excitation of only specific molecular orientations in pulsed EPR[33]. Because the intramolecular signal is sensitive to the orientations of the inter-spin vector with respect to the applied magnetic field, the interpretation of distance measurements becomes convoluted since a single experiment cannot properly sample all orientations. This effect is generally referred to as orientational selectivity[18,26,34]. Note that orientational selectivity also occurs in other pulsed-EPR methods that probe electron-nuclear interactions[35–38]. These effects also apply to other spin systems, such as Co(II)[39], Fe cation[40–44], and even Tyrosine radicals[45], with anisotropy in their spectra. Due to orientational selectivity with rigid Cu(II)-labels, pulsed-EPR distance measurements require multiple acquisitions at different positions of the Cu(II) spectrum as an attempt to sample all Cu(II) orientations completely[18]. In response, our group has established a DEER acquisition scheme that is 6-fold faster[46] than a previous scheme[18]. This acquisition scheme allows for proper orientation sampling of the Cu(II)-labeled protein with only ca. 10% excitation of the Cu(II) spectrum.

While simulations validated the acquisition scheme, there remained several limitations. Specifically, the simulations assumed idealistic rectangular inversion profiles. However, realistic pulses have inversion pulses that deviate from a perfect rectangular inversion. Additionally, with the recent development of shaped pulses, the inversion profiles vary among different types of pulses. Overall, understanding how different pulses affect orientational selectivity is lacking, yet crucial for pushing the limit of commercial spectrometers. In addition, the earlier work did not systematically optimize the frequency offset between the two pulses used in the double resonance experiment.

In this work, we used simulations to explore these effects for orientation-independent distance measurement. Specifically, we implemented a new procedure that can incorporate inversion profiles of realistic pulses for Double Electron-Electron Resonance (DEER) experiments[5,6]. Additionally, we demonstrate how the optimal frequency offsets between observer and pump frequencies depend on the angle between the two orientations of the Cu(II) spins. Moreover, by combining the rectangular pulses and a judiciously determined frequency offset, we show that orientation-independent DEER distance measurements can be achieved in just two DEER experiments, which removes the need for an additional experiment from the acquisition protocol[18,46]. Next, we show that increasing the power of the rectangular pulses can lead to DEER experiments with almost three-fold higher sensitivity. Finally, we demonstrate the applicability of the acquisition scheme for two separate proteins to showcase the robustness of the acquisition scheme.

Experimental

Generation of in-silico sample

To make an in-silico sample, we used a home-written Python[47] code that generated 50,000 sets of three vectors representing $g_\parallel$-axes of two Cu(II) spins (Spin A and Spin B) and the interspin vector, $\boldsymbol{r}$. The relative orientations of the three vectors were defined using χ, γ, and η[33]. The parameter χ represents the angle between the $g_\parallel$-axis of Spin A and $\boldsymbol{r}$, γ represents the angle between the two $g_\parallel$-axes of Spin A and Spin B, and η represents the angle between the $g_\perp$-axes of Spin A and Spin B. Each of χ, γ, and η were sampled using Gaussian distributions with user-defined means and a $10°$ standard deviation for all three angles. The $10°$ standard deviation is a reasonable lower estimate for the rigid dHis-Cu(II) label, as previously shown[1,15,18]. A comprehensive analysis of several cases of χ, γ, and η is discussed in the Results section and in ESI. In addition to the three angles, we sampled the magnitude of $\boldsymbol{r}$ from a Gaussian distribution with a mean of 5.2 nm and a standard deviation of 0.05 nm. The small standard deviation is the lowest limit of the breadth of distance distribution observed for dHis-Cu(II)[14]. Furthermore, a mean of 5.2 nm is long enough that a 0.1 nm variation can cause a discernable 159 ns difference in the dipolar modulation period. The combination of a long mean and a small standard deviation represents a system more prone to orientational selectivity than real dHis-Cu(II) labeled proteins.

After the generation of 50,000 spin-pairs, we tabulated the orientations of the $g_\parallel$-axis of each spin with respect to the applied magnetic field, ϕ. This angle is crucial for obtaining properties that are unique to each spin. The ϕ angle of a spin dictates the effective g and A-values, as follows[48]:

$$g(\phi) = \sqrt{g_\perp^2 \sin^2 \phi + g_\parallel^2 \cos^2 \phi} \quad \text{EQ.1}$$

$$A(\phi) = \frac{\sqrt{A_\perp^2 g_\perp^4 \sin^2 \phi + A_\parallel^2 g_\parallel^4 \cos^2 \phi}}{g_\perp^2 \sin^2 \phi + g_\parallel^2 \cos^2 \phi} \quad \text{EQ.2}$$

We used the $g_\parallel = 2.277$, $g_\perp = 2.057$, $A_\parallel = 162$ G, and $A_\perp = 10$ G, which are canonical for the dHis-Cu(II)[3,49].

In addition to ϕ, we tabulated the orientation of $\boldsymbol{r}$ with respect to the applied magnetic field, θ. The angle θ affects the magnetic dipolar interaction of each spin-pair, as follows:

$$\nu_{ee} = \frac{\mu_0 g_A g_B \beta_e^2}{4\pi h r^3}(3\cos^2(\theta) - 1) \quad \text{EQ.3}$$

where ν_{ee} is the magnetic dipolar frequency of the interaction between the two spins, μ_0 is the vacuum magnetic permeability, and g_A or g_B represents the g-value of Spin A or Spin B.

Simulation of the dHis-Cu(II) spectum

The dHis-Cu(II) spectrum represents B_{res} from all of the dHis-Cu(II) spins in the sample. However, due to unresolved splittings and molecular strains, an EPR spectrum manifests as broadened line shapes rather than discrete lines[50,51]. Therefore, we calculated a Lorentzian line shape for each B_{res,m_l} of a spin in the in-silico sample as follows:

$$I_\phi(B) = \sum_{m_l} \frac{\beta^2}{(B - B_{res,m_l})^2 + \beta^2} \quad \text{EQ.4}$$

where β is a broadening parameter for the Lorentzian lineshape. The β value was chosen to be 40 G, as previously published[46]. We generated a dHis-Cu(II) spectrum of the in-silico sample by summing all lineshapes.

More importantly, we tabulated the set of excitable spins at each field, described as follows:

$$X(B) = \{\phi \in U | I_\phi(B) \geq \alpha\} \quad \text{EQ.5}$$

where $X(B)$ represents the set of spins excitable at the magnetic field B, U represents all ϕ angles in the in-silico sample, and α is a threshold parameter. The parameter α dictates whether the intensity of the spectral lineshape is considered significant or not. This threshold is crucial since EQ.4 provides a non-zero value for all field values. We consider a spin excitable if the intensity of the spin's spectral lineshape at that field is above α. More details of this approach are available in earlier work[46]. In this work, α was set as 0.4, as previously established[46]. Overall, EQ.5 describes the set of spins that resonate at a specific magnetic field.

Protein sample preparation

We used two proteins in this work. The first system is a 15H/17H/28H/32H variant of the immunoglobulin binding domain of protein G (GB1). The GB1 mutant was expressed and purified as previously published work[52,53]. The second protein is the S-hexylglutathione (GSHex)-bound human Glutathione S-Transferase A1-1 (hGSTA1-1). The expression and purification of hGSTA1-1 mutant 211H/215H used a previously published protocol[2,46,54], while the ligand, GSHex, was purchased from Sigma Aldrich. The purified proteins were concentrated and aliquoted to ~200 μM in pH = 6.5 buffer with 150 mM NaCl and 50 mM sodium phosphate and stored at -80 °C. For labeling, Cu(II) chelated to nitrilotriacetic acid (NTA) was used to ensure selective binding[55]. We prepared a 10 mM Cu(II)NTA stock using published protocol[49,56]. The choice of MOPS buffer allows for efficient Cu(II)NTA binding to dHis-motifs in the proteins used[49]. Preparation of each protein sample used a 1:1 ratio of Cu(II)NTA to dHis-motif in 50 mM MOPS and 100 mM NaCl in D$_2$O (pH = 7.4). Regarding hGSTA1-1, GSHex was added with 1:1 stoichiometry with the protein before adding Cu(II)NTA. We incubated the samples at 4 °C for 35 min. Finally, we added 40% of deuterated glycerol, and the final solution was flash-frozen in liquid methylacetylene-propadiene propane (MAPP) gas. A step-by-step protocol for spin labeling and flash freezing is available in literature[56].

EPR measurements

Dead-time free 4-pulse DEER[6] experiments at Q-band frequencies were performed at 18 K using a Bruker ElexSys FT/CW spectrometer with either Bruker ER5106-QT2 resonator or Bridge12 resonator and a 300 W amplifier. To maintain stable cryogenic temperature, an Oxford CF935 dynamic continuous-flow cryostat attached to Oxford LLT 650 low-loss transfer tube and an Oxford ITC503 temperature controller were used. The following pulse sequence was used: $(\pi/2)\nu_A$-τ-$(\pi)\nu_A$-τ+t -$(\pi)\nu_B$ -T-t-$(\pi)\nu_A$-T-echo. The exact pulse length and type used are described in the results section for each experiment. For GB1, the initial values of T was 1200 ns and t was -200 ns. Then, t was incremented by a step size of 10 ns over 140 points. For hGSTA1-1, the initial value for T was 6500 ns and t was -400 ns. The variable t was incremented by a step size of 26 ns over 266 points. A 16-step phase cycling was used to remove unwanted signal[6]. All DEER experiments were done by setting the pump frequency at 124 G and 803 G lower than the maximum of the Cu(II) spectrum unless stated otherwise. The DEER signals were normalized to the intensity of the Electron Spin Echo Field Swept (ESE-FS) spectrum and summed together to obtain the final DEER signal. ConsensusDEERAnalysis (CDA)[57,58] was used to analyze the data.

Results and Discussion

The intramolecular DEER signal is given by EQ.6:

$$V_{intra}(t) =$$

$$\int_{r_{min}}^{r_{max}} \int_{0°}^{90°} \lambda(1 - \cos(2\pi\nu_{ee}t))P(\theta)P(r) \, d\theta dr \quad \text{EQ.6}$$

where λ is the modulation depth of the signal, ν_{ee} is the frequency of the intramolecular magnetic dipolar interaction of the two spins, and θ is the angle between the applied magnetic field and the interspin vector, $\boldsymbol{r}$. In EQ.6, sampling of all statistical orientations in the powder sample leads to $P(\theta) = sin\theta$. When a DEER experiment fails to sample all orientations properly, $P(\theta)$ deviates from $\sin(\theta)$, and orientational selectivity will occur, which can lead to improper extraction of the distance distribution. Additionally, orientational selectivity affects the amplitude of the DEER signal, λ[34]. The theory describing orientational selectivity is well understood[59] and demonstrated for nitroxides and Cu(II) labels[18,40,59–76]. However, the analytical formalism cannot, in general, provide information on θ values sampled [i.e., $P(\theta)$] by an orientational selective DEER at a given field, creating a bottleneck for analysis. Therefore, we recently developed a different approach using an in-silico analysis to simulate DEER experiments[46]. The in-silico sample allows for direct identification of the spin-pairs and the corresponding θ angles and $P(\theta)$ at a given magnetic field. With this approach, we can evaluate the proper sampling of θ to obtain orientation-independent DEER measurements.

For any given sample, we modeled each spin-pair on a protein as a set of three vectors; two vectors for the direction
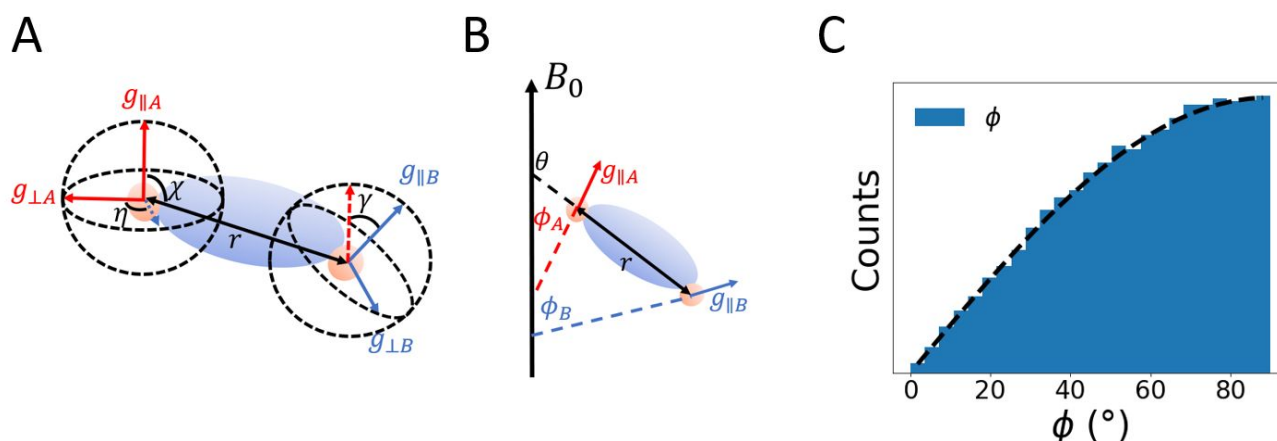
Fig. 1. A) Representation of a Cu(II)-labeled protein as a set of three vectors corresponding to the $g_∥$ of the two spins and the interspin vector, r. The relative orientations of the three vectors are described by angles $χ$, $γ$, and $η$. **B)** Relative to the applied magnetic field, the orientation of $g_∥$ for each of the two spins are denoted with $φ$, while the orientation of r is denoted by $θ$. **C)** All $φ$ angles of the *in-silico* sample were calculated and plotted as a histogram, and overlaid with the expected $sin(φ)$ distribution, depicted with a dashed black line.

of the $g_∥$ of Spin A and Spin B and the inter-spin vector, r, as shown in Figure 1A. We describe the orientations of the $g_∥$-axis of the spins and r with respect to the applied magnetic field as $φ$ and $θ$, respectively, as shown in Figure 1B. Note that for any rigid label system, $θ$ is correlated with $φ$ in a manner that depends on the relative orientations of the g-tensors and r. The angular relationships between the three vectors with three parameters, $χ$, $γ$, and $η$[33], are depicted in Figure 1A. Note that these three angular parameters that describe the relative orientations of the g-tensors depend on the position of the labeled sites. These relative orientations for many systems are not known a *priori*, and therefore the analytical description of $θ$ is hard to define as a function of $φ$. On the other hand, we can easily estimate the $φ$ angles of the excited spins in a DEER experiment as they only depend on the resonant field and the precise values of g- and hyperfine tensors, which are typically available. More importantly, proteins in a powder or frozen solution have the same statistical distribution of $φ$, shown in Figure 1C. Therefore, this work aims to properly sample $P(θ)$ by optimizing the excitation of $φ$.

Generation of in-silico sample

For the first step, we generated 50,000 randomly oriented vectors representing doubly dHis-Cu(II)labeled proteins. For each molecule, $χ$, $γ$, and $η$ are sampled from gaussian distributions with means of 90°, 45°, and 90° respectively. We chose these angular parameters to model two dHis-Cu(II) labels on opposite sides of a simple $β$-barrel protein[77]. The $β$-barrel fold is a promising starting model since approximately 600 proteins adopt this architecture[78]. Note that this choice of the mean angles is only an arbitrary starting case. We explore other relative orientations in later sections. Each Gaussian distribution has a standard deviation of 10°.

A standard deviation of 10° for $χ$, $γ$, $η$ is a conservative estimate for the dHis-Cu(II) label[15,18]. Once generated, we randomly rotate each doubly-labeled protein to simulate the orientations of a powder or frozen solution sample.

Excitation of a spin with a given $φ$ angle depends on the resonant fields, calculated as follows[48]:

$$B_{res,m_l}(φ) = \frac{hν - A(φ)m_l}{g(φ)β_e} \qquad \text{EQ.7}$$

where h is the Planck constant, $ν$ is the microwave frequency, m_l is the nuclear quantum number, and $β_e$ is the Bohr Magneton. Note that the effective g and A values depend on $φ$, easily calculated using EQ.1 and EQ.2 in the Methods section. As such, we calculated B_{res} for each spin in the in-silico sample using EQ.7. These resonant fields were stored to identify which spins were excited at a specific magnetic field in the dHis-Cu(II) spectrum (cf. Methods section). After the generation of the in-silico sample, we implemented a procedure that samples the spins in the in-silico sample given any pulse.

Sampling of $φ$ angles by rectangular pulses primarily depends on the bandwidth of the major lobe in the inversion profile

To identify the sampled $φ$ angles, we calculated the inversion profiles of a rectangular pulse and a pulse with uniform excitation over a specific range. Figure 2A shows the inversion profile of a 20 ns rectangular pulse in the dashed black line compared to a pulse that uniformly excites spins over a 100 MHz bandwidth. The 20 ns rectangular pulse has a sinc inversion profile, calculated using the Exciteprofile and Pulse functions[79] of EasySpin[51]. This profile provides the probability of exciting spins as a function of the magnetic field, $P(B)$. At the central field, the probability of 1 corresponds to all spins being excited. At other fields, only a portion of the spins gets excited. In contrast, the uniform excitation pulse assumes an inversion profile with a probability of 1 across a 33.57 Gauss range, representing a perfect bandwidth of 100 MHz. The assumption of a uniform excitation over a 100 MHz bandwidth was used in previous work[46]. While the uniform excitation pulse allows for a straightforward calculation since a spin is either excited or not, the rectangular pulse better represents experiments accessible for any commercial pulsed-EPR spectrometer. We note that the calculated inversion profile ignores experimental distortions due to resonator bandwidths, B_1 inhomogeneity, and video
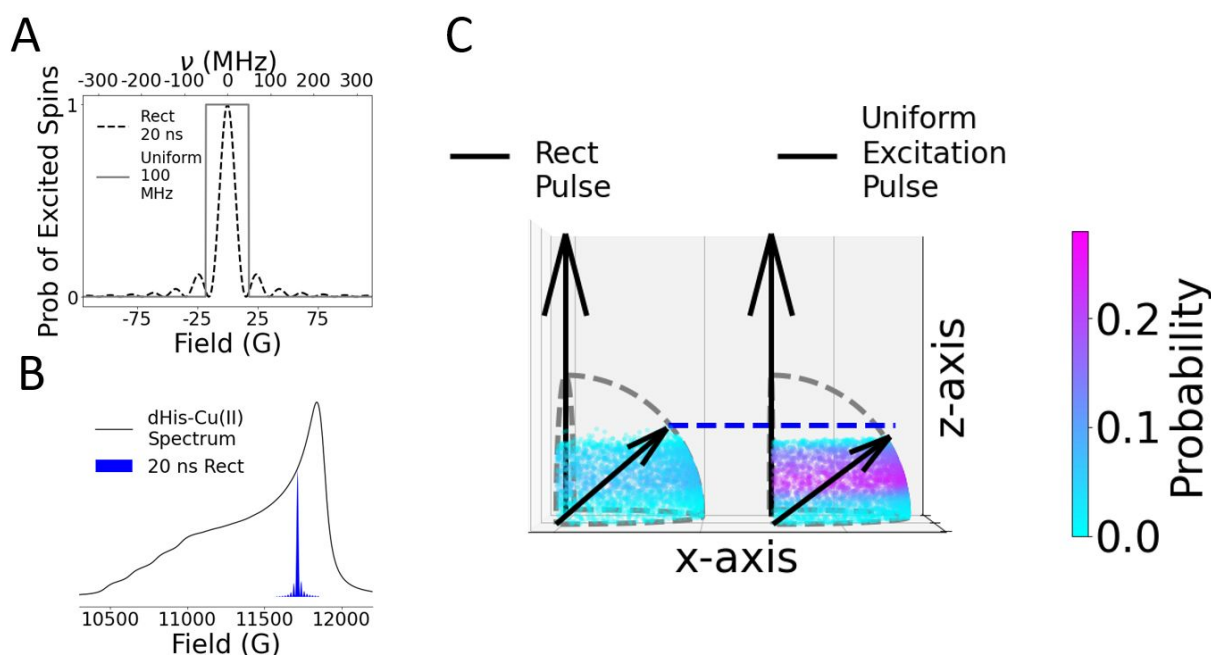
Fig. 2 A) Functions for the probability of spin excitation as a function of either field or frequency relative to the pulse frequency were calculated from the inversion profiles of two pulses. The sinc inversion profile of a 20 ns rectangular pulse was calculated using EasySpin[51], and is depicted with a black dashed line. The other inversion profile describes a pulse with uniform excitation across a 100 MHz band and is depicted with a solid grey line. **B)** To contextualize the sinc inversion profile produced by the 20 ns rectangular pulse, the inversions profile is overlayed in blue on a field swept spectrum calculated from the *in-silico* sample in grey. The pulse is centred at 124 G lower than the maximum of the Cu(II) spectrum. **C)** The identified spins by the rectangular and uniform excitation pulses are shown as a scatter plot, color-coded by the probability of the excited spin. The coordinates of each dot correspond to the ϕ angle of each spin in cartesian coordinates. The axial black arrow depicts the applied magnetic field in the z-direction. Overall, the rectangular pulse excites a lower probability of spins than the ones excited by the uniform excitation pulse but has a slightly larger range. The lower probability is due to the imperfect sinc inversion profile of the rectangular pulse.

amplifier bandwidths, that can alter the experimentally observed inversion profile[80–83]. We discuss the effect of this contribution later while discussing experimental results. While Figure 2A only shows one example of a rectangular pulse, the method can be applied to any pulse and pulse length. These results are shown in Figure S1.

For demonstration, Figure 2B shows a rectangular pulse set at a central magnetic field 11715 G, shown as the shaded blue region. The inversion profile is overlaid on a simulated dHis-Cu(II) absorption spectrum shown as the black line in Figure 2B. The simulated dHis-Cu(II) spectrum was constructed by summing the resonant fields of all spins in the in-silico sample, as described in the Methods section. Overall, the pulse covers only a small range of magnetic fields compared to the dHis-Cu(II) spectrum. As a result, the pulse excites only a limited number of the spins in the in-silico sample.

A spin is excited when the spectral lineshape of the spin, $I_\phi(B)$, overlaps with the probability curve of the pulse, $P(B)$. We obtained the spectral lineshape $I_\phi(B)$ by applying Lorentzian broadening of the resonant fields of the spins, described in EQ.4 in the Methods section. The overlap between the spectral lineshape of a spin and the pulse region signifies that the pulse has a non-zero probability of exciting that particular spin. Therefore, the pulse excites only spins with resonant fields in the shaded blue region in Figure 2B. Figure 2C shows the excited spins as a scatter plot where the polar coordinates of each dot correspond to the ϕ angle of a spin.

The color-coding on each dot in Figure 2C represents the probability of exciting each spin, calculated as follows:

$$P(\phi_n) = \frac{\int I_\phi(B)P(B)\,dB}{\int I_\phi(B)\,dB} \quad \text{EQ.8}$$

EQ.8 calculates the probability of exciting spin n with a given ϕ as the portion of the spectral lineshape, $I_\phi(B)$, that overlaps with the pulse probability curve, $P(B)$. Figure 2C shows that the rectangular pulse excites spins with a ~5° larger range of ϕ angles than those sampled by the uniform excitation pulse. The 5° increase in the range of ϕ angles is due to the minor lobes of the sinc inversion profile, shown in Figure 2A. On the other hand, the rectangular pulse excites the spins with a smaller probability than a pulse with the uniform excitation pulse. We can rationalize the lower probability due to the imperfect inversion from the sinc profile of the rectangular pulse. On the other hand, sophisticated shaped pulses, such as CHIRP and hyperbolic secant pulses[84,85], are closer to uniform inversion than rectangular pulses, as shown in Figure S1. Overall, this method of implementing pulses allows for the sampling of spins in the in-silico sample, given a realistic inversion profile of any pulse.

To explore the effect of pulse types, we calculated the distribution of ϕ of excited spins at three different fields in the dHis-Cu(II) spectrum. Figure 3A marks the three fields in gray circles, and Figures 3B-3D show the corresponding ϕ angles of the excited spins. In each plot, the solid gray line and the dashed black line represent the ϕ angles of the spins excited by the
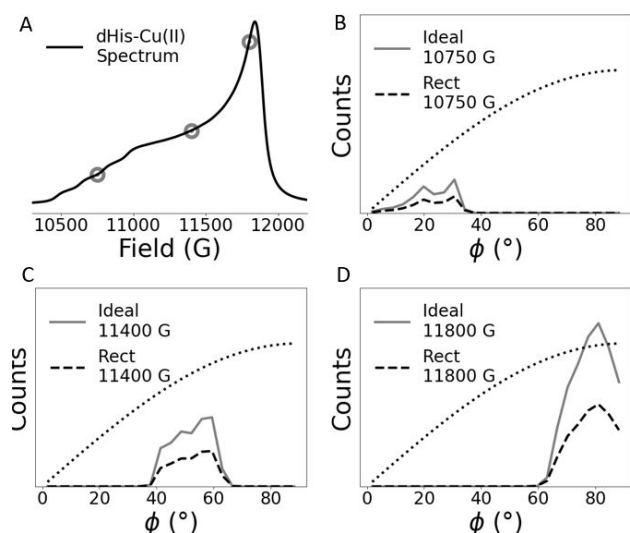
Fig. 3. A) A 20 ns rectangular pulse and a uniform excitation 100MHz pulse were set at three different fields across the dHis-Cu(II) spectrum, marked by the grey circles. At each field, the excited ϕ angles were calculated and plotted for the rectangular and uniform excitation pulse, represented as the dashed black line and the solid gray line, respectively. The distributions of excited ϕ angles are shown in panels **B-D**. Complete excitation of all ϕ angles was expected to follow a sinusoidal trend, depicted as dotted black lines. The two pulses excite similar ranges of ϕ angles, and the only difference between the two pulses is the intensity of the ϕ excitation.

uniform excitation pulse and the rectangular pulse, respectively. The ϕ angle distributions are based on $P(\phi)$ of each excited spin, as calculated by EQ.8. The pulses at different fields excite spins with different sets of ϕ angles. In each case, the distribution of ϕ follows the trend of the dHis-Cu(II) spectrum in Figure 3A. For example, Figure 3B shows a bimodal distribution corresponding to the two peaks surrounding the 10750 G point in Figure 3A. Similarly, the distribution at 11400 G shows an upward slope similar to the trend in the dHis-Cu(II) spectrum. Finally, the sharp peak in Figure 3D matches the sharp feature at 11800 G of the dHis-Cu(II) spectrum. These observations are within expectation since the dHis-Cu(II) spectrum reflects the statistical distribution of ϕ angles at different magnetic fields.

Interestingly, as ϕ shifts to 0°, the intensity of excited spins gets significantly less than the expected $P(\phi)$, depicted as the dotted black line in Figures 3B-3D. At ϕ angles near 0°, the effective hyperfine values, $A(\phi)$, are close to the $A_{\parallel}$ value of ~161 G, leading to large splitting. Since the pulse primarily excites a range of ~40 G based on Figure 2A, the pulse excites only a small portion of the spins with ϕ values near 0°. As a result, under-sampling of the $P(\phi)$ occurs at lower ϕ angles.

The rectangular pulse has a more prominent under-sampling than the uniform excitation pulse. The intensity difference of the spin excitation between the two pulses is within expectation since they have different inversion profiles, as predicted by Figure 2C. Additionally, Figure 2C indicates a slight increase in the range of ϕ angles due to the minor lobes of the rectangular pulse. However, the difference in ϕ angles is small, making it hard to observe in Figures 3B-3D. The difference is only apparent when the $P(\phi)$ curves from the two pulses are

normalized to each other, as shown in Figure S2. Therefore, the minor lobes contribute minimally to the excitation of ϕ angles.

These results indicate that the central lobe of the rectangular pulse is the main contributor to the excitation of the Cu(II) spins. The main lobe covers the same ~40 G region as the 100 MHz uniform excitation pulse, as shown in Figure 2A. As a result, both pulses effectively excite spins with similar ranges of ϕ angles, as shown in Figure 3. Furthermore, the pulse still excites similar ϕ angles even after the contribution from the resonator bandwidth, as shown in Figure S3. On the other hand, the imperfection of the rectangular pulse reduces $P(\phi)$ to approximately half of its uniform excitation counterpart. Therefore, rectangular and shaped pulses with near-rectangular profiles excite spins with similar ϕ angles, albeit with different efficiencies.

The frequency offset between observer and pump pulses dictates the orientations of Spin A and Spin B

Next, we identified the most optimal field for exciting the greatest number of unique ϕ angles. In Figure 4A, we plot the number of unique ϕ angles of the excited spins at each field, referred to as the Φ-curve. This quantification was done by setting the rectangular pulse at each field and tabulating the corresponding ϕ angles of the excited spins. From the Φ-curve, we observed a maximum, marked by a blue dot. The Φ-curve maximum resides at 124 G lower than the maximum of the Cu(II) spectrum, consistent with previous work[46]. The difference in the Φ-curve maximum and the spectrum maximum is due to the large $A_{\parallel}$ of the dHis-Cu(II) compared to $A_{\perp}$. Thus, spins with ϕ angles as low as 60° still have resonant fields at the Φ-curve maximum, as shown in Figure S4. On the other hand, the range of ϕ values at the spectrum maximum is much narrower. Therefore, DEER experiments at the spectrum maximum are not optimal in Cu(II) systems with orientational selectivity.

The Φ-curve calculation in Figure 4A uses the arbitrary model of dHis-Cu(II)-labeled β-barrel protein as a starting case. However, the Φ-curve depends on the statistical distribution of the ϕ angles of the spins, which is independent of the relative orientations of the g-tensors. Therefore, the Φ-curve maximum provides excitation of spins with the largest range of ϕ angles, regardless of the system.

While the Φ-curve establishes the most optimal field for a single pulse, DEER is a two-frequency experiment that uses pump and observer pulses. Figure 4B shows a pump pulse (red) set at the Φ-curve maximum and an observer pulse (blue) set at Δv away from the pump pulse. Next, we identified all spins excited by the pump and observer pulses, respectively. The approach is shown schematically in Figure 4C. The pumped and observed spin are shown as red and blue circles, respectively. With this method, we isolated all molecules where one spin was pumped while the other was observed. For each spin-pair, we stored the values of ϕ and θ. In addition, we used the precise values of r and θ to calculate the contribution of each spin-pair to DEER. With this method, we further analyzed the ϕ angles of the spins excited by the two pulses separated by different frequency offsets, Δv.
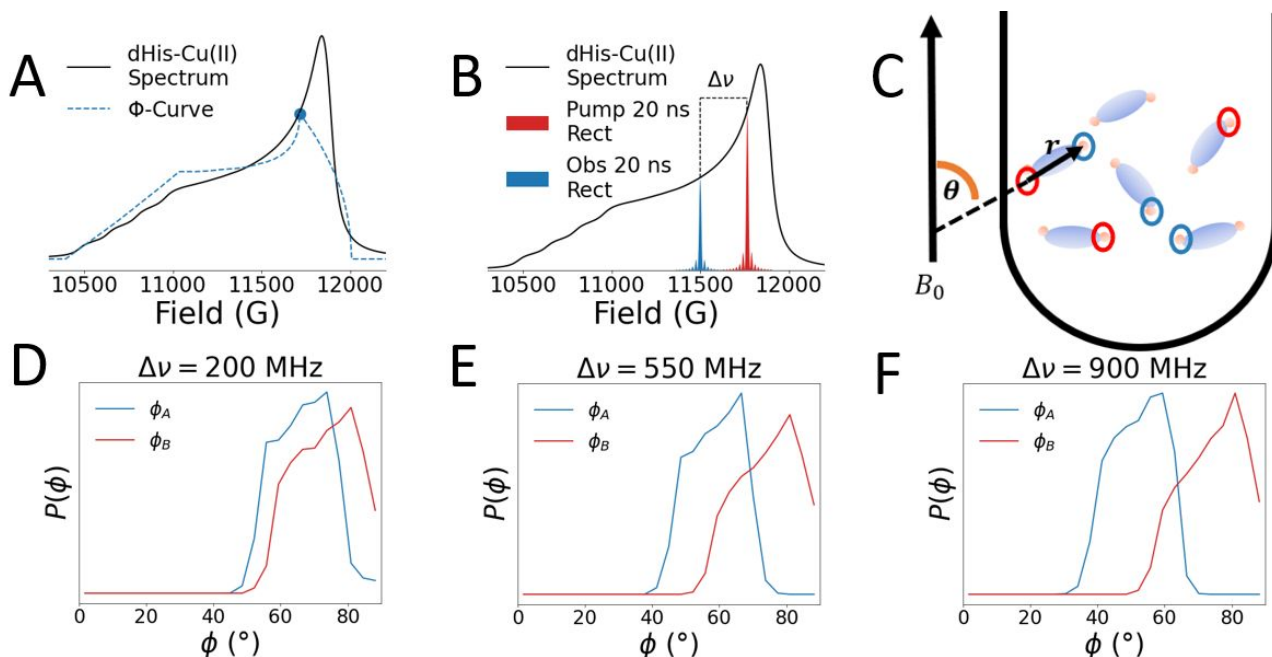
Fig. 4. A) The number of unique ϕ angles excited at each field (dashed blue line) labeled as the Φ-curve. The maximum of the Φ-curve is marked by the blue dot. **B)** DEER simulations were performed by simulating the pump pulse set at the maximum of the Φ-curve and the observer pulse set at different frequency offsets, $\Delta\nu$, from the pump pulse. **C)** The pump and observer pulses excite different spins, marked by red and blue circles, respectively. Only protein molecules with both spins excited by the two pulses were considered for the intramolecular DEER signal. Plots of the ϕ angles in the spin-pairs excited by either the observer (ϕ_A) or the pump pulse (ϕ_B) are shown for $\Delta\nu$ of **(D)** 200 MHz, **(E)** 550 MHz, and **(F)** 900 MHz. As $\Delta\nu$ increases, the observer pulse excites lower ϕ_A angles since lower angles have lower resonant fields.

For a specific $\Delta\nu$, we identified the excited spin-pairs and plotted the ϕ angles of Spin A and Spin B excited by the observer and pump pulses, labeled as ϕ_A and ϕ_B, respectively. Figures 4D-4F show the distributions of ϕ_A and ϕ_B, depicted as blue and red lines, respectively. For $\Delta\nu$ of 900 MHz, Figure 4F shows the distribution of ϕ_A centered at a lower angle compared to the ϕ_A in the 200 MHz case. This difference is expected since increasing $\Delta\nu$ shifts the observer pulse to lower field where lower ϕ angles resonate. As a result, a larger $\Delta\nu$ leads to the excitation of a more extensive range of ϕ angles in total. However, as is evident in Figure 4F, increasing $\Delta\nu$ to 900 MHz reduces the sampling of spins with ϕ angles of ~65° with the observer pulse.

Excitation of the intramolecular interaction is dependent on the relative orientations of the two spins

Given the relationship of ϕ and θ (cf. Figure 1A), we expect that optimizing $\Delta\nu$ plays a critical role in the efficient sampling of θ values of the excited spin-pairs. As per Figure 1, the correlation between ϕ and θ is dependent on the relative orientation between r and the $g_\parallel$-axes of the two spins, defined by χ, γ, and η[33]. Therefore, we explored how the three angles affect the number of sampled θ angles. Figure 5 shows that γ significantly affects the sampling of θ angles.

Figure 5 shows five cases where γ varies by increments of 20°, depicted by the different orientations of Spin B, shown as the green arrow. In each case, we identified the excited spin-pairs as described in Figure 4 and quantified the number of sampled θ with varying $\Delta\nu$ values. The right panels of Figure 5 show the scatter plot of the number of the sampled θ angles as a function of $\Delta\nu$ for each case of γ. When γ is 0°, both the $g_\parallel$-axes of Spin

A and Spin B are parallel to each other. In this case, the sampling of θ is the highest when the $\Delta\nu$ is as small as possible, based on the scatter plot in Figure 5A. This observation is expected since both spins have the same orientation and resonant field.

As γ increases to 40°, the most optimal $\Delta\nu$ shifts to ~400 MHz, as shown in Figure 5C. In this case, the directions of the two spins deviate enough that their resonant fields start to differ significantly. Consequently, optimal excitation of the spin-pair requires the observer and pump frequencies to also differ by the same extent as the difference in the resonant fields of the two spins. Finally, Figure 5E shows the extreme case where the largest γ leads to the largest difference in the directions of Spin A and Spin B. Therefore, the optimal $\Delta\nu$ is at 1900 MHz for this case to accommodate the large difference in the resonant fields of the two spins. While Figure 5 explores γ from 0° to 90°, Figure S5 shows that γ angles from 90° to 180° also exhibit identical patterns. These results show that the optimal $\Delta\nu$ primarily depends on the difference between ϕ_A and ϕ_B.

In contrast to γ, variation in either χ or η have minimal effect on the sampling of θ, as shown in Figures S6 and S7. In Figure 1A, the χ angle dictates the orientation of r with respect to the $g_\parallel$-axis of Spin A. However, Figure 5 indicates that the excitation of spin pairs primarily depends on both ϕ_A and ϕ_B. Because ϕ_B has no relationship with χ, the number of sampled θ angles is independent of the angle χ. On the other hand, the variation of η is effectively an axial rotation between Spin A and B, as shown in Figure 1A. However, octahedrally coordinated Cu(II) is an axial g-tensor system. As a result, an axial rotation of the spins does not affect the resonant field of the spin. Thus, the η parameter minimally affects the resonant fields of Spin A

ARTICLE

Journal Name
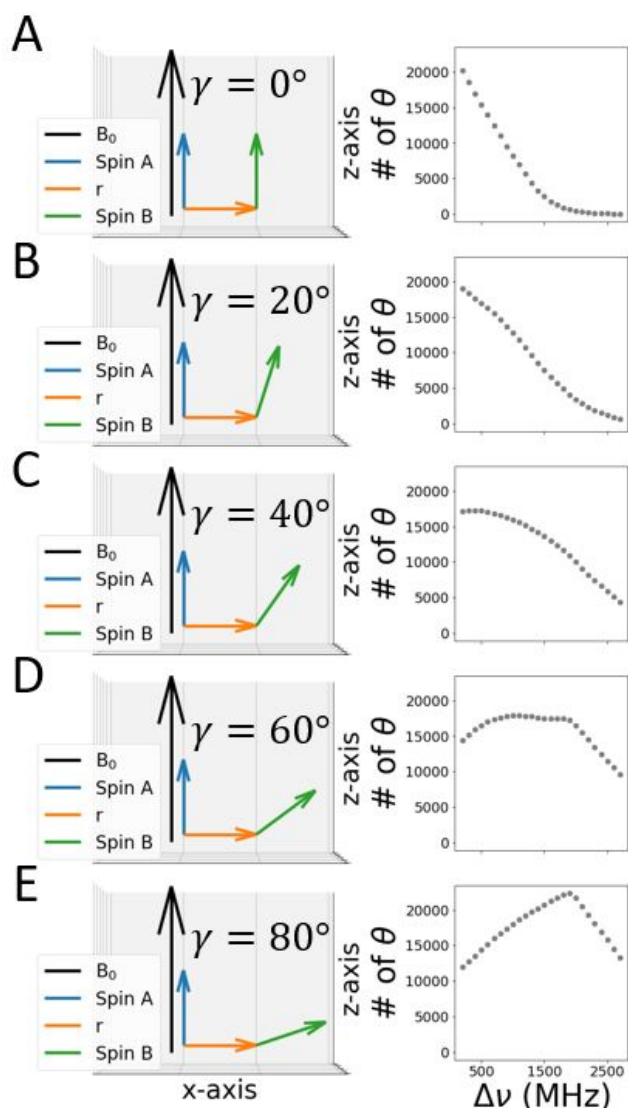
Fig. 5. Analysis of five different cases where the angle between the $g_{\parallel}$-axes of the two spins was incremented by 20°, defined by the parameter γ. The organization of r and the two $g_{\parallel}$-axes of the spins are depicted on the left panels as orange, blue, and green, respectively. DEER simulations were done on each case with a variety of $\Delta\nu$ values. The number of excited θ as a function of $\Delta\nu$ is plotted as gray dots on the right panels. The optimal $\Delta\nu$ varies in each case. As the orientations of the two spins deviate, the optimal $\Delta\nu$ increases to properly excite the two spins with differing resonant fields.

and Spin B. Overall, only the parameter γ affects the number of excited spin-pairs, while χ and η do not.

These results conceptually explain how λ in EQ.6 is also affected by orientational selectivity[34]. The variable λ is proportional to the amount of spin-pairs excited by a pulsed-EPR experiment[6]. By exciting more spin-pairs, a DEER experiment also samples more θ angles in the sample. As shown in Figures 4 and 5, the relative orientation of the system and $\Delta\nu$ affect the efficiency of sampling θ angles, which correlates with the efficiency of exciting spin-pairs in the sample. As a result, the prediction of λ in an unknown orientational selective system is more challenging than those without orientational selectivity[5,30,86,87]. Overall, these results provide an additional

physical basis for the complicated relationship between orientational selectivity and the many facets of DEER.

Frequency offset of 300 MHz enables orientation-independent distance measurement with two DEER experiments

Based on Figure 5, there is no perfect choice of $\Delta\nu$ that can optimally sample θ angles in all cases. Additionally, given realistic limitations, performing DEER at extremely low $\Delta\nu$ leads to problematic ESEEM effects in the signal[6], while extremely high $\Delta\nu$ requires specialized equipment[88–91]. Therefore, we considered a $\Delta\nu$ of 300 MHz that is accessible in common resonators. Additionally, this $\Delta\nu$ seems to be a reasonable compromise that does not minimally or maximally sample θ angles in all cases explored in Figure 5.

To explore whether proper $P(\theta)$ is achievable, we simulated a DEER experiment using the two-pulse approach, as described in Figures 4B and 4C, with a $\Delta\nu$ of 300 MHz. Additionally, we used the β-barrel protein with χ, γ, and η of 90°, 45°, and 90°, respectively, as a preliminary example. Figure 6A shows the dHis-Cu(II) spectrum and the Φ-curve in the dashed blue line. The blue dot represents the field position, $B_{\phi0}$, of the pump pulse, which is a 20 ns rectangular pulse. Additionally, we set a 20 ns rectangular observer pulse at a lower field position, 300 MHz away from the pump pulse. With these two pulses, we identified the excited spin-pairs and the corresponding sampled θ angles. Note that the excitations of Spin A and Spin B have probabilities of $P(\phi_A)$ and $P(\phi_B)$, respectively, calculated using EQ.8. Therefore, we weighted each sampled θ angle by multiplying $P(\phi_A)$ and $P(\phi_B)$ in each excited spin-pair. Figure 6B shows the distribution of sampled θ angles as the blue histogram. Compared to the expected $P(\theta)$, we still undersample the θ angles above 50°. Therefore, a single DEER at $B_{\phi0}$ is insufficient for sampling $P(\theta)$ with such a pulse, and excitation of the leftover spin-pairs requires additional experimentation.

To obtain another position for the second DEER simulation, we eliminated the excited spin-pairs at $B_{\phi0}$, and then plotted a new Φ-curve from the leftover spin-pairs, Iteration 1, depicted in the dashed orange line in Figure 6A. A new Φ-curve maximum, $B_{\phi1}$, is marked as the orange dot at 803 G lower than the maximum of the dHis-Cu(II) spectrum. Figure 6B shows the total distribution of the sampled θ after the second DEER as the orange histogram. The additional DEER leads to the sampling of θ angles above 50°, providing better agreement between the expected $P(\theta)$ and the total sampled θ angles.

With the sampled θ, we then simulated the expected intramolecular DEER signal, calculated as follows:

$$V_{intra}(t) = \sum_{i=1}^{N} P(\phi_{Ai})P(\phi_{Bi})\cos(2\pi\nu_{eei}t) \quad \text{EQ.9}$$
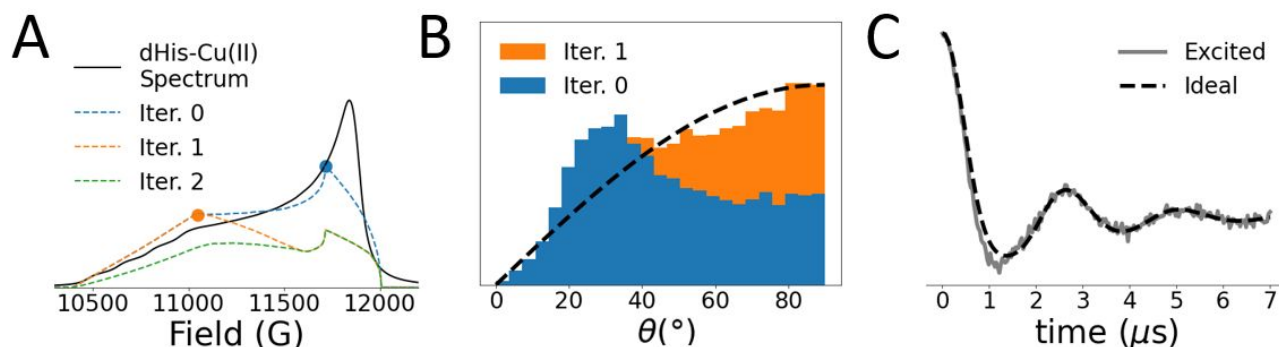
Fig. 6. **A)** Φ-curve analysis, where the DEER simulations used Φ-curve 300 MHz. Each iteration is a Φ-curve obtained from spin pairs that were not yet excited by DEER simulations from previous iterations. The maximum of each Φ-curve, marked by colored dots, was identified as the most promising field for simulating DEER at a given iteration. **B)** The distribution of excited θ from the simulated DEER performed at the fields shown in panel A after each iteration. **C)** The simulated DEER signal after performing the DEER experiments at the fields identified in panel A compared to the ideal case where all spins are excited. These results show that acquisition of DEER at two fields can potentially provide orientationally averaged DEER signal.

where N is the number of excited spin-pairs, t is the dipolar evolution time, $P(\phi_A)$ and $P(\phi_B)$ are the excitation probability of Spin A and Spin B, and ν_{ee} is the magnetic dipolar frequency of the interaction between the two spins. Calculation of ν_{ee} is described in the methods section. EQ.9 assumes a pure intramolecular signal and does not account for λ. Additionally, both $P(\theta)$ and $P(r)$ are naturally accounted for in the terms $P(\phi_{Ai})P(\phi_{Bi})$ and ν_{ee}. Figure 6C shows the simulated DEER signal as a gray line. For comparison, we also calculated the ideal DEER signal using EQ.9 by assuming the excitation of all spin-pairs in the in-silico sample, shown as the dashed black line. Overall, the simulated DEER signal is within the noise of the ideal DEER signal, as shown in Figure 6C. These simulations suggest that $\Delta\nu$ of 300 MHz is sufficient at sampling θ with <u>two</u> DEER experiments.

While Figure 6 shows promising calculations, we also explored whether increasing $\Delta\nu$ can lead to efficient θ sampling by a single DEER simulation. Simulations with larger $\Delta\nu$ are shown in Figures S8 and S9. Overall, a single DEER still manifests orientational selectivity even when $\Delta\nu$ is 3 GHz, large enough to observe at $g_\parallel$ and pump at $g_\perp$ of the dHis-Cu(II) spectrum. However, if $\Delta\nu$ decreases to 200 MHz or below, collecting three DEER signals becomes necessary, as illustrated in the ESI.

This observation is consistent with previous work that assumed 200 MHz frequency offsets for DEER experiments[46]. Even when pulses have 800 to 1200 MHz bandwidths, proper θ sampling is still unachievable with a single DEER. Details are provided in Figure S11. The simulations support previous work that showed orientational selectivity even when using Ultra-Wideband pulses and powerful loop-gap resonators[32]. Therefore, we conclude that orientational-independent distance measurements require $\Delta\nu$ of at least 300 MHz, leading to a minimum acquisition scheme of *two DEER experiments*.

New acquisition scheme provides orientation-independent distance measurements for most cases of relative orientations

Note that the simulation in Figure 6 is an analysis for a single case of χ=90°, γ=45°, and η=90°. Therefore, we tested the robustness of the two fields identified from the 300 MHz

simulations in Figure 6A to all possible combinations of χ, γ, and η. To simulate different proteins, we systematically incremented the three angles by 20°. We simulated the DEER signal based on $B_{\phi 0}$ and $B_{\phi 1}$ for each combination of χ, γ, and η. Figure 7 shows the simulated DEER signal, depicted as the gray line, for all cases of χ and γ while η value is 0°. Cases for other η angles are shown in Figures S12-S15. Overall, we tested 125 possible combinations of χ, γ, and η. Each DEER signal was combined with simulated noise to replicate an SNR of 50. Figure 7 shows the simulated DEER signals within the noise of the ideal DEER signal, shown as the dashed black line, for most cases. However, 10 out of 125 cases still manifest small deviations
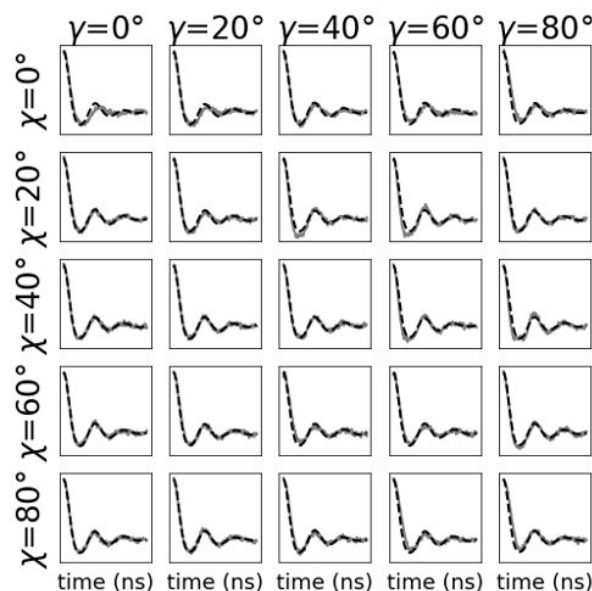
Fig. 7. The simulated and ideal DEER time traces were obtained for different angles of χ and γ while η is 0°. The simulated DEER was obtained using the two identified fields in Figure 6A, given a 300 MHz frequency offset between observer and pump frequencies. Acquisition of DEER at two fields leads to properly account for orientations is general for several relative orientations of the g tensors of the two electron spins.

between the simulated DEER signal and the ideal signal. These deviations can lead to a minor distribution appearing in the
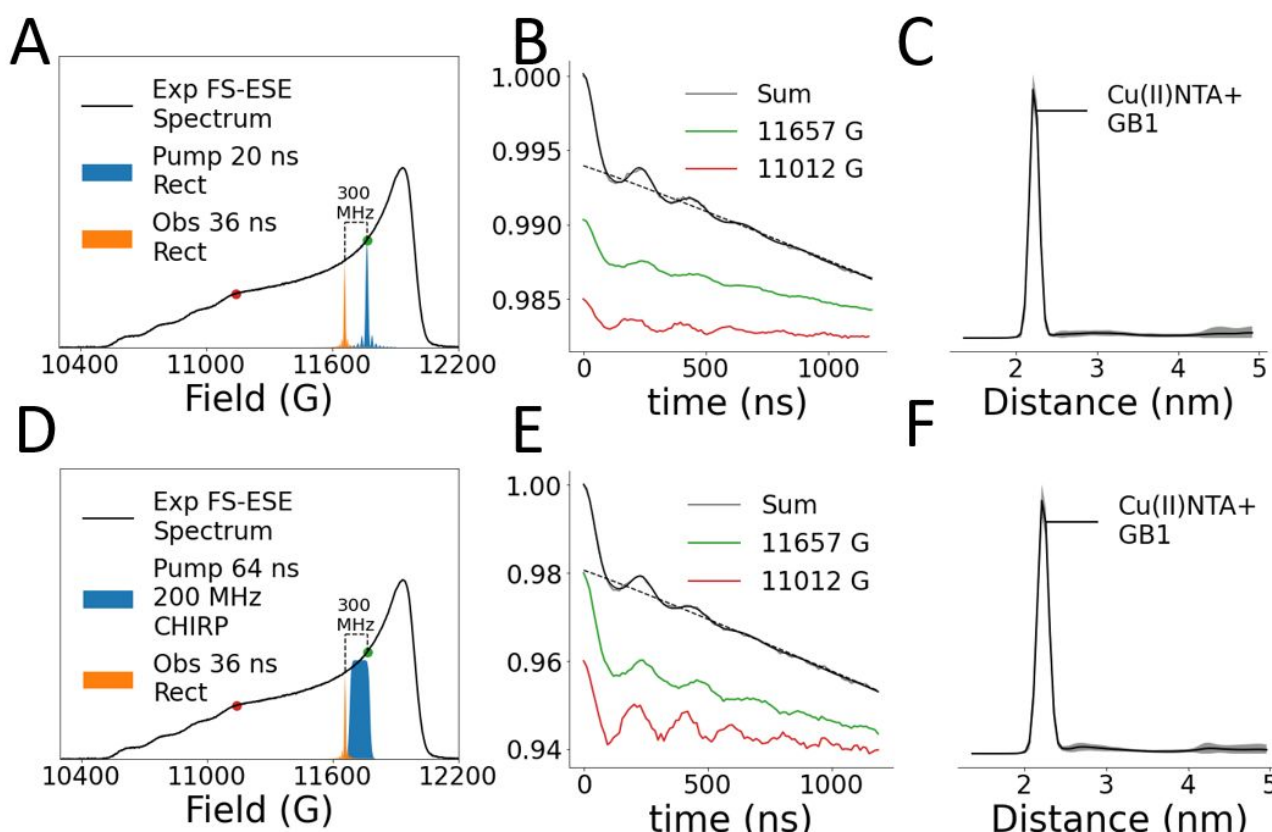
Fig. 8. A) DEER setup on a QT2 resonator using a 36 ns rectangular observer pulse and a 20 ns rectangular pump pulse set at 300 MHz away from the observer frequency on Cu(II)NTA labeled GB1. The experiment was done at two positions marked by the green and red dots. The FS-ESE spectrum of dHis-Cu(II) was collected at 34.693 GHz. **B)** The DEER signal for the respective fields and the sum of these signals in black, overlayed with the background fit dashed black line. **C)** The distance distribution obtained from the summed DEER signal in black, with grey shading to represent error. **D)** The DEER experiment was repeated using a 64 ns 200 MHz CHIRP pump pulse. **E)** & **F)** The corresponding DEER signal and the distance distribution are shown in E and F, respectively. These results demonstrate the experimental validation for the two-field acquisition scheme.

extracted distance distribution, as discussed in previous work[46]. In these cases, two additional fields at the spectrum maximum and 500 G lower than the maximum of the spectrum may be needed. More details are shown in ESI.

Orientational-averaged DEER is achievable with either rectangular or CHIRP pulses

To further validate the simulations, we performed DEER experiments on 15H/17H/28H/32H GB1 mutant. This mutant has two sites that contain two strategically placed histidine residues (dHis motif)[14]. Each dHis motif can coordinate with Cu(II) chelated by nitrilotriacetic acid (NTA)[55] or iminodiacetic acid (IDA)[92]. The Cu(II) chelation allows Cu(II) to bind preferentially to the dHis motifs. Furthermore, efficient incorporation of Cu(II)NTA to the dHis motifs of 15H/17H/28H/32H GB1 mutant has already been established[20,49]. Therefore, this dHis-Cu(II) labeled system is suitable to test the simulations performed in this work.

To replicate the 300 MHz frequency offset simulation, we first used the QT2 resonator from Bruker. Figures 8A and 8D show the observer and pump pulses, depicted as the orange and blue regions, used for the two DEER experiments. The pump pulse was either a 20 ns rectangular pulse or a 64 ns 200 MHz CHIRP. Given the anticipated distance of 2.3 nm, a longer CHIRP

pump pulse is not recommended[85]. In both cases, the observer pulse was a 36 ns rectangular pulse. The rectangular pump pulse was 300 MHz away from the observer frequency. In the other case, the 200 MHz CHIRP pump pulse was centered at 200 MHz from the observer frequency. Overall, in both cases, the pulses were within the resonator bandwidth of QT2. We performed the DEER for both cases at ca. 124 G and 803 G lower than the maximum of the FS-ESE spectrum. These positions are shown as green and red dots in Figures 8A and 8D. While the pulse parameters differ from those used in previous sections, DEER simulations based on pulses used in Figures 8A and 8D also support the ability of the acquisition scheme to provide an orientation-independent measurement. These results are provided in Figure S17 in ESI.

Figures 8B and 8E show the DEER signals at 124 G and 803 G, color-coded green and red, respectively. The gray line is the sum of both DEER signals. The summing procedure is described in the methods section. From the summed DEER signal, we observed a modulation depth (λ) of 0.6% when the pump pulse is a 20 ns rectangular pulse while a 200 MHz CHIRP pump pulse provides λ of 1.8%. This three-fold difference in λ makes sense since the 200 MHz CHIRP excites more spins than a 20 ns rectangular pulse. The summed DEER signals were analyzed using Consensus DEER Analysis (CDA)[57,58] to extract the distance
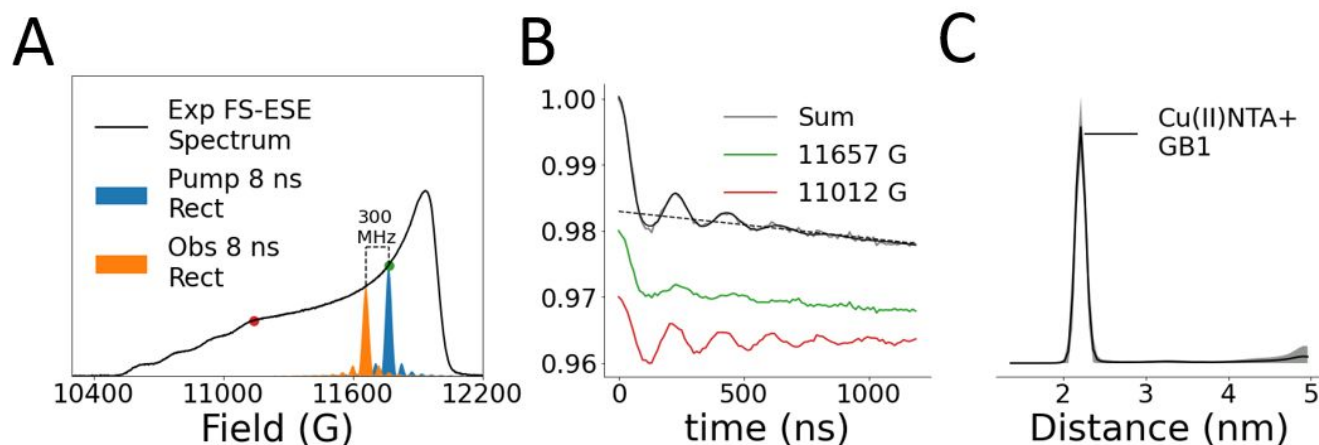
Fig. 9. A) DEER setup on a B12 resonator using an 8 ns rectangular pulse for both observer and pump pulses separated by 300 MHz on a Cu(II)NTA labeled GB1 protein. The experiment was done at two positions marked by the green and red dots. The FS-ESE spectrum of dHis-Cu(II) was collected at 34.693 GHz. **B)** The DEER signal for the respective fields and the sum of these signals in black, overlayed with the background fit dashed black line. **C)** The distance distribution between labels obtained from the summed DEER signal in black, with grey shading to represent error. The distribution is in agreement with the data in Figure 8. More importantly the use of shorter pulse lengths and resonator volume enabled the measurement of distances from ca. five times lower spins.

distribution. Figures 8C and 8F show the distance distributions. In both cases, the distance distributions are within experimental errors, with a most probable distance of 2.3 nm. This distance is consistent with previous measurements on this Cu(II) labeled GB1 mutant[14,17,18,55,92].

Thus, the experimental results validate the simulations showing that proper orientation sampling is achievable in two DEER experiments with $\Delta\nu$ of 300 MHz. Second, rectangular pump pulses have the same capability as CHIRP pulses to provide orientation-independent distance measurements. This result is not unexpected since both rectangular and uniform excitation pulses excite spins with similar ranges of ϕ angles (cf. Figures 2 and 3). These results are significant given the widespread prevalence of spectrometers that only support rectangular pulses.

Shortening of rectangular pulses increases the sensitivity of the DEER experiment

While QT2 can sufficiently sample θ, we explored whether increasing the power of the pulses can improve the efficiency of orientation-independent DEER experiments. Specifically, we performed DEER using another commercially available Bridge12 QLP (B12) resonator. This resonator increases the strength of the pulse by using a loop-gap resonator which, on our spectrometer, enables pi pulses of 8 ns (cf. Figure S18). Therefore, this resonator can excite more spins using rectangular pulses compared to the Bruker QT2 resonator.

We performed DEER on dHis-Cu(II) labeled GB1 using the B12 resonator at the two fields marked by the green and red dots in Figure 9A. At each position, we used 8 ns rectangular pulses with a 300 MHz frequency offset between the observer and pump frequency. The pulse positions are shown in Figure 9A. Figure 9B shows the DEER signals at the two fields as green and red lines, while the summed signal is shown as a gray line. The 8 ns rectangular pump pulse leads to a summed DEER signal with a λ of 1.6%. This λ from the 8 ns rectangular pulse is about

2.7-fold higher than the λ obtained when using a 20 ns pump pulse, shown in Figure 8B. More importantly, the increased power of the rectangular pulse provided λ comparable to the 1.8% seen in the QT2 DEER using a CHIRP pump pulse, shown in Figure 8D. Additionally, the DEER distance measurements with the B12 resonator require a 5-fold less absolute number of spins compared to the experiment with the QT2 resonator, given the smaller resonator volume. However, despite the reduced number of spins, the DEER echo in B12 was comparable to the DEER echo obtained in the QT2 resonator (cf. as shown in Figure S19 in ESI). Therefore, the B12 resonator allows for sensitive distance measurements with rectangular pulses while reducing the number of proteins required in the sample.

Orientation-independent distance measurement is robust to different proteins

To further demonstrate the robustness of the acquisition scheme for different systems, we performed a DEER experiment on another protein, hGSTA1-1. We expressed and purified
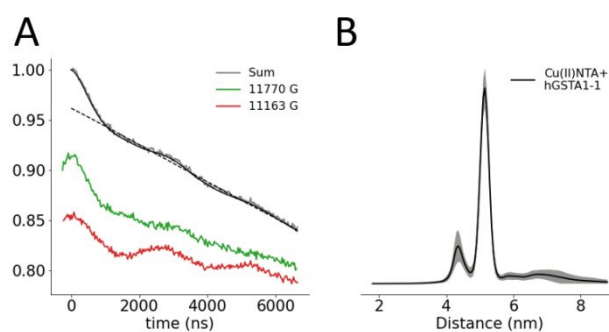
Fig. 10. A) DEER signals obtained using a B12 resonator, a 16 ns rectangular pulse as the observer pulse and a 250 ns 250 MHz CHIRP pump pulse separated by 150 MHz. This was done at two fields on Cu(II)NTA labeled hGSTA1-1. The sum of the two signals is depicted in black and is overlayed with the background fit dashed black line. **B)** The distance distribution obtained from the summed DEER signal is depicted black, with error in grey. These results further validate the generality of the two-field acquisition scheme.

K211H/E215H hGSTA1-1 as previously described[2,54]. The protein hGSTA1-1 is a homodimer; thus, one dHis mutant is sufficient to provide two Cu(II)NTA labeling sites for DEER experiments. Furthermore, we prepared hGSTA1-1 in the presence of stoichiometric amounts of GS-Hex ligand[93].

We performed DEER on the hGSTA1-1 sample using the B12 resonator. Figure 10A shows the DEER signal from the two fields as green and red lines, while the summed DEER signal is shown as a grey line. We note that the summed DEER signal has λ of 4%, significantly higher than the λ in the GB1 DEER experiments. The significant improvement in λ is due to using a 250 ns 250 MHz CHIRP pump pulse.

Figure 10B shows the extracted distance distribution by CDA[57,58]. The measured distance distribution has the most probable distance at 5.3 nm, consistent with previous work using the same hGSTA1-1 mutant[46]. Additionally, the distribution has a minor distance of around 4.2 nm. Previous work also observed the minor peak, even when DEER experiments were done at ten different fields at Q-band or performed at X-band (where orientation effects are not observed for this label)[46].

These results demonstrate that DEER can be optimized to minimize the number of experiments required to achieve orientationally averaged DEER. On the other hand, previous efforts involved systematic collection of DEER measurements at many magnetic fields across the Cu(II) spectrum[18,32,33,62]. This procedure benefits from automation[94] while providing additional data to extract orientational information. However, DEER experiments at lower fields generally have low echo intensity and low λ, leading to long experimental run time to achieve sufficient SNR. As a result, high quality DEER at multiple fields requires disproportionate allotment of the overall experimental time, skewing heavily towards the low magnetic fields. In contrast, this work shows that one can invest less time by performing DEER experiments at a select few magnetic fields, reducing the experimental run time by as much as 6-fold[18].

Conclusions

In this work, we showcase an approach for simulating orientational selectivity in the context of Cu(II)-DEER experiments. Simply, this approach consists of three modular parts; creating vectors that represent any type of spins or interactions, defining the Hamiltonian of the desired system, and the pulses that replicate the desired experiment. Each vector is then interrogated to establish its contribution to the signal and the molecular orientation. Such a strategy provides a means to calculate the spectrum and, more importantly, extract information on the orientational dependence. We show that a rectangular pulse can sample similar spin orientations, albeit with a lower probability, as a pulse with perfect excitation across the same bandwidth of the rectangular pulse. Additionally, we provide a further understanding of the relationship between frequency offsets and the number of excited spin-pairs. This physical exploration helps rationalize how orientational selectivity affects the amplitude of the intramolecular dipolar signal in DEER. Through a comprehensive analysis of all possible cases of relative orientations, we establish a new acquisition scheme that requires only two DEER experiments with frequency offsets of 300 MHz for orientation-independent distance measurements. Furthermore, increasing the power of the rectangular pulse allows for DEER experiments with comparable sensitivity to experiments using CHIRP pulses. Finally, the new acquisition scheme works for multiple systems, as validated by the experimental results of GB1 and hGSTA1-1 distance measurements.

The approach demonstrated in this work is an early concept applicable not only to DEER experiments but also to RIDME[95–97], ESEEM[35], ENDOR[36,38,43,98], HYSCORE[37], and ELDOR-detected NMR[99]. These techniques probe interactions containing an orientation-dependent component at the molecular level while limited by current pulse capabilities. This approach provides a supplementary analysis tool to several existing software to simulate orientational selective data[33,51,100–103], in order to comprehensively associate orientational selectivity with different techniques, molecular models, and experimental parameters. Future expansion of the in-silico sample approach may further reveal hidden details and assist with interpreting these pulsed-EPR techniques.

Author Contributions

Z.H. performed the experiments, analyzed the data, and wrote the Python program for carrying out the simulations. N.A.M. analyzed the theoretical results and contributed to implementing realistic pulses into the Monte-Carlo Simulations. S.S. conceived the project and supervised all aspects of the work. Z.H., N.A.M, and S.S. prepared the manuscript. All authors reviewed the manuscript and agreed to the final version of the manuscript.

Conflicts of interest

There are no conflicts to declare.

Acknowledgements

Notes and references

1. A. Gamble Jarvi, X. Bogetti, K. Singewald, S. Ghosh, and S. Saxena, *Acc. Chem. Res.*, 2021, **54**, 1481–1491.
2. K. Singewald, X. Bogetti, K. Sinha, G. S. Rule, and S. Saxena, *Angew. Chem. Int. Ed.*, 2020, **59**, 23040–23044.
3. K. Singewald, H. Hunter, T. F. Cunningham, S. Ruthstein, and S. Saxena, *Analysis & Sensing*, 2022.
4. P. P. Borbat and J. H. Freed, *Chem. Phys. Lett.*, 1999, **313**, 145–154.
5. A. D. Milov, A. B. Ponomarev, and Y. D. Tsvetkov, *Chem. Phys. Lett.*, 1984, **110**, 67–72.

6.   M. Pannier, S. Veit, A. Godt, G. Jeschke, and H. W. Spiess, *J. Magn. Reson.*, 2000, **142**, 331–340.

7.   S. Milikisyants, F. Scarpelli, M. G. Finiguerra, M. Ubbink, and M. Huber, *J. Magn. Reson.*, 2009, **201**, 48–56.

8.   L. V. Kulik, S. A. Dzuba, I. A. Grigoryev, and Y. D. Tsvetkov, *Chem. Phys. Lett.*, 2001, **343**, 315–324.

9.   G. Jeschke, M. Pannier, A. Godt, and H. W. Spiess, *Chem. Phys. Lett.*, 2000, **331**, 243–252.

10. M. Bonora, J. Becker, and S. Saxena, *J. Magn. Reson.*, 2004, **170**, 278–283.

11. W. L. Hubbell, C. J. López, C. Altenbach, and Z. Yang, *Curr. Opin. Struct. Biol.*, 2013, **23**, 725–733.

12. P. Widder, J. Schuck, D. Summerer, and M. Drescher, *Phys. Chem. Chem. Phys.*, 2020, **22**, 4875–4879.

13. D. Goldfarb, *Phys. Chem. Chem. Phys.*, 2014, **16**, 9685–9699.

14. T. F. Cunningham, M. R. Putterman, A. Desai, W. S. Horne, and S. Saxena, *Angew. Chem. Int. Ed.*, 2015, **54**, 6330–6334.

15. X. Bogetti, S. Ghosh, A. Gamble Jarvi, J. Wang, and S. Saxena, *J. Phys. Chem. B*, 2020, **124**, 2788–2797.

16. H. Sameach, S. Ghosh, L. Gevorkyan-Airapetov, S. Saxena, and S. Ruthstein, *Angew. Chem. Int. Ed.*, 2019, **58**, 3053–3056.

17. J. Casto, A. Mandato, and S. Saxena, *J. Phys. Chem. Lett.*, 2021, **12**, 4681–4685.

18. A. Gamble Jarvi, K. Ranguelova, S. Ghosh, R. T. Weber, and S. Saxena, *J. Phys. Chem. B*, 2018, **122**, 10669–10677.

19. A. Gamble Jarvi, T. F. Cunningham, and S. Saxena, *Phys. Chem. Chem. Phys.*, 2019, **21**, 10238–10243.

20. J. L. Wort, K. Ackermann, A. Giannoulis, A. J. Stewart, D. G. Norman, and B. E. Bode, *Angew. Chem. Int. Ed.*, 2019, **58**, 11681–11685.

21. K. Ackermann, J. L. Wort, and B. E. Bode, *Chem. Commun.*, 2022, **58**, 8790–8793.

22. M. Oranges, J. L. Wort, M. Fukushima, E. Fusco, K. Ackermann, and B. E. Bode, *J. Phys. Chem. Lett.*, 2022, **13**, 7847–7852.

23. M. J. Lawless, J. L. Sarver, and S. Saxena, *Angew. Chem. Int. Ed.*, 2017, **56**, 2115–2117.

24. S. Ghosh, M. J. Lawless, H. J. Brubaker, K. Singewald, M. R. Kurpiewski, L. Jen-Jacobson, and S. Saxena, *Nucleic Acids Res.*, 2020, **48**, e49.

25. J. Casto, A. Mandato, L. Hofmann, I. Yakobov, S. Ghosh, S. Ruthstein, and S. Saxena, *Chem. Sci.*, 2022, **13**, 1693–1697.

26. D. M. Engelhard, A. Meyer, A. Berndhäuser, O. Schiemann, and G. H. Clever, *Chem. Commun.*, 2018, **54**, 7455–7458.

27. L. M. Stratmann, Y. Kutin, M. Kasanmascheff, and G. H. Clever, *Angew. Chem. Int. Ed.*, 2021, **60**, 4939–4947.

28. M. P. Donohue and V. A. Szalai, *Phys. Chem. Chem. Phys.*, 2016, **18**, 15447–15455.

29. S. R. Sweger, V. P. Denysenkov, L. Maibaum, T. F. Prisner, and S. Stoll, *Magn. Reson.*, 2022, **3**, 101–110.

30. Z. Yang, M. Ji, and S. Saxena, *Appl Magn Reson*, 2010, **39**, 487–500.

31. A. Doll and G. Jeschke, *J. Magn. Reson.*, 2014, **246**, 18–26.

32. F. D. Breitgoff, K. Keller, M. Qi, D. Klose, M. Yulikov, A. Godt, and G. Jeschke, *J. Magn. Reson.*, 2019, **308**, 106560.

33. Z. Yang, D. Kise, and S. Saxena, *J. Phys. Chem. B*, 2010, **114**, 6165–6174.

34. R. G. Larsen and D. J. Singel, *J. Chem. Phys.*, 1993, **98**, 5134–5146.

35. H. L. Flanagan, G. J. Gerfen, A. Lai, and D. J. Singel, *J. Chem. Phys.*, 1988, **88**, 2162–2168.

36. A. Kehl, M. Hiller, F. Hecker, I. Tkach, S. Dechert, M. Bennati, and A. Meyer, *J. Magn. Reson.*, 2021, **333**, 107091.

37. T. Iwasaki, A. Kounosu, T. Uzawa, R. I. Samoilova, and S. A. Dikanov, *J. Am. Chem. Soc.*, 2004, **126**, 13902–13903.

38. G. H. Rist and J. S. Hyde, *J. Chem. Phys.*, 1970, **52**, 4633–4643.

39. M. Baumgarten, C. J. Winscom, and W. Lubitz, *Appl Magn Reson*, 2001, **20**, 35–70.

40. A. M. Bowen, E. O. D. Johnson, F. Mercuri, N. J. Hoskins, R. Qiao, J. S. O. McCullagh, J. E. Lovett, S. G. Bell, W. Zhou, C. R. Timmel, L. L. Wong, and J. R. Harmer, *J. Am. Chem. Soc.*, 2018, **140**, 2514–2527.

41. Y. Kim, J. Kim, L. K. Nguyen, Y.-M. Lee, W. Nam, and S. H. Kim, *Inorg. Chem. Front.*, 2021, **8**, 3775–3783.

42. M. M. Roessler, M. S. King, A. J. Robinson, F. A. Armstrong, J. Harmer, and J. Hirst, *Proc. Natl. Acad. Sci. USA*, 2010, **107**, 1930–1935.

43. G. E. Cutsail, J. Telser, and B. M. Hoffman, *Biochim. Biophys. Acta*, 2015, **1853**, 1370–1394.

44. D. Abdullin, F. Duthie, A. Meyer, E. S. Müller, G. Hagelueken, and O. Schiemann, *J. Phys. Chem. B*, 2015, **119**, 13534–13542.

45. A. V. Astashkin, H. Hara, and A. Kawamori, *J. Chem. Phys.*, 1998, **108**, 3805–3812.

46. X. Bogetti, Z. Hasanbasri, H. R. Hunter, and S. Saxena, *Phys. Chem. Chem. Phys.*, 2022, **24**, 14727–14739.

47. R. G. Van and F. Drake, *Scotts Valley, CA: CreateSpace*, 2009, **10**, 1593511.

48. W. R. Hagen, *Biomolecular EPR Spectroscopy*, CRC Press, 2008.

49. A. Gamble Jarvi, J. Casto, and S. Saxena, *J. Magn. Reson.*, 2020, **320**, 106848.

50. A. I. Smirnov and R. L. Belford, *Journal of Magnetic Resonance, Series A*, 1995, **113**, 65–73.

51. S. Stoll and A. Schweiger, *J. Magn. Reson.*, 2006, **178**, 42–55.

52. T. F. Cunningham, S. Pornsuwan, W. S. Horne, and S. Saxena, *Protein Sci.*, 2016, **25**, 1049–1060.

53. T. F. Cunningham, M. S. McGoff, I. Sengupta, C. P. Jaroniec, W. S. Horne, and S. Saxena, *Biochemistry*, 2012, **51**, 6350–6359.

54. M. J. Lawless, J. R. Pettersson, G. S. Rule, F. Lanni, and S. Saxena, *Biophys. J.*, 2018, **114**, 592–601.

55. S. Ghosh, M. J. Lawless, G. S. Rule, and S. Saxena, *J. Magn. Reson.*, 2018, **286**, 163–171.

56. K. Singewald, J. A. Wilkinson, and A. S. Saxena, *Bio Protoc*, 2021, **11**, e4258.

57. S. G. Worswick, J. A. Spencer, G. Jeschke, and I. Kuprov, *Sci. Adv.*, 2018, **4**, eaat5218.

58. L. Fábregas Ibáñez, G. Jeschke, and S. Stoll, *Magn. Reson.*, 2020, **1**, 209–224.

59. A. G. Maryasov, Y. D. Tsvetkov, and J. Raap, *Applied Magnetic Resonance*, 1998, **14**, 101–113.

60. Z. Yang, J. Becker, and S. Saxena, *J. Magn. Reson.*, 2007, **188**, 337–343.

61. B. E. Bode, J. Plackmeyer, T. F. Prisner, and O. Schiemann, *J. Phys. Chem. A*, 2008, **112**, 5064–5073.

62. A. M. Bowen, M. W. Jones, J. E. Lovett, T. G. Gaule, M. J. McPherson, J. R. Dilworth, C. R. Timmel, and J. R. Harmer, *Phys. Chem. Chem. Phys.*, 2016, **18**, 5981–5994.
63. K. Halbmair, J. Seikowski, I. Tkach, C. Höbartner, D. Sezer, and M. Bennati, *Chem. Sci.*, 2016, **7**, 3172–3180.
64. M. Heinz, N. Erlenbach, L. S. Stelzl, G. Thierolf, N. R. Kamble, S. T. Sigurdsson, T. F. Prisner, and G. Hummer, *Nucleic Acids Res.*, 2020, **48**, 924–933.
65. A. Marko, V. Denysenkov, D. Margraf, P. Cekan, O. Schiemann, S. T. Sigurdsson, and T. F. Prisner, *J. Am. Chem. Soc.*, 2011, **133**, 13375–13379.
66. L. S. Stelzl, N. Erlenbach, M. Heinz, T. F. Prisner, and G. Hummer, *J. Am. Chem. Soc.*, 2017, **139**, 11674–11677.
67. C. M. Grytz, A. Marko, P. Cekan, S. T. Sigurdsson, and T. F. Prisner, *Phys. Chem. Chem. Phys.*, 2016, **18**, 2993–3002.
68. N. Erlenbach, B. Endeward, P. Schöps, D. B. Gophane, S. T. Sigurdsson, and T. F. Prisner, *Phys. Chem. Chem. Phys.*, 2016, **18**, 16196–16201.
69. T. F. Prisner, A. Marko, and S. T. Sigurdsson, *J. Magn. Reson.*, 2015, **252**, 187–198.
70. A. M. Bowen, C. E. Tait, C. R. Timmel, and J. R. Harmer, in *Structural Information from Spin-Labels and Intrinsic Paramagnetic Centres in the Biosciences*, eds. C. R. Timmel and J. R. Harmer, Springer Berlin Heidelberg, Berlin, Heidelberg, 2013, vol. 152, pp. 283–327.
71. J. E. Lovett, A. M. Bowen, C. R. Timmel, M. W. Jones, J. R. Dilworth, D. Caprotti, S. G. Bell, L. L. Wong, and J. Harmer, *Phys. Chem. Chem. Phys.*, 2009, **11**, 6840–6848.
72. A. M. Bowen, A. Bertran, K. B. Henbest, M. Gobbo, C. R. Timmel, and M. Di Valentin, *J. Phys. Chem. Lett.*, 2021, **12**, 3819–3826.
73. I. Kaminker, I. Tkach, N. Manukovsky, T. Huber, H. Yagi, G. Otting, M. Bennati, and D. Goldfarb, *J. Magn. Reson.*, 2013, **227**, 66–71.
74. K. Halbmair, J. Wegner, U. Diederichsen, and M. Bennati, *Biophys. J.*, 2016, **111**, 2345–2348.
75. G. Sicoli, T. Argirević, J. Stubbe, I. Tkach, and M. Bennati, *Appl Magn Reson*, 2010, **37**, 539–548.
76. M. V. Fedin, G. Y. Shevelev, D. V. Pyshnyi, V. M. Tormyshev, G. Jeschke, M. Yulikov, and E. G. Bagryanskaya, *Phys. Chem. Chem. Phys.*, 2016, **18**, 29549–29554.
77. T. Páli and D. Marsh, *Biophys. J.*, 2001, **80**, 2789–2797.
78. Y. Lu, N. Yeung, N. Sieracki, and N. M. Marshall, *Nature*, 2009, **460**, 855–862.
79. S. Stoll and R. D. Britt, *Phys. Chem. Chem. Phys.*, 2009, **11**, 6614–6625.
80. P. E. Spindler, P. Schöps, W. Kallies, S. J. Glaser, and T. F. Prisner, *J. Magn. Reson.*, 2017, **280**, 30–45.
81. P. E. Spindler, Y. Zhang, B. Endeward, N. Gershernzon, T. E. Skinner, S. J. Glaser, and T. F. Prisner, *J. Magn. Reson.*, 2012, **218**, 49–58.
82. T. E. Skinner, M. Braun, K. Woelk, N. I. Gershenzon, and S. J. Glaser, *J. Magn. Reson.*, 2011, **209**, 282–290.
83. T. E. Skinner, T. O. Reiss, B. Luy, N. Khaneja, and S. J. Glaser, *J. Magn. Reson.*, 2004, **167**, 68–74.
84. A. Tannús and M. Garwood, *Journal of Magnetic Resonance, Series A*, 1996, **120**, 133–137.
85. P. E. Spindler, S. J. Glaser, T. E. Skinner, and T. F. Prisner, *Angew. Chem. Int. Ed.*, 2013, **52**, 3425–3429.
86. Y. D. Tsvetkov, A. D. Milov, and A. G. Maryasov, *Russian Chemical Reviews*, 2008.
87. B. E. Bode, D. Margraf, J. Plackmeyer, G. Dürner, T. F. Prisner, and O. Schiemann, *J. Am. Chem. Soc.*, 2007, **129**, 6736–6745.
88. V. Denysenkov, P. van Os, and T. F. Prisner, *Appl Magn Reson*, 2017, **48**, 1263–1272.
89. J. W. Sidabras, T. Sarna, R. R. Mett, and J. S. Hyde, *J. Magn. Reson.*, 2017, **282**, 129–135.
90. J. S. Hyde, J. W. Sidabras, and R. R. Mett, *Cell Biochem. Biophys.*, 2019, **77**, 3–14.
91. R. Tschaggelar, F. D. Breitgoff, O. Oberhänsli, M. Qi, A. Godt, and G. Jeschke, *Appl Magn Reson*, 2017, **48**, 1273–1300.
92. M. J. Lawless, S. Ghosh, T. F. Cunningham, A. Shimshi, and S. Saxena, *Phys. Chem. Chem. Phys.*, 2017, **19**, 20959–20967.
93. D. C. Kuhnert, Y. Sayed, S. Mosebi, M. Sayed, T. Sewell, and H. W. Dirr, *J. Mol. Biol.*, 2005, **349**, 825–838.
94. I. Kaminker, M. Florent, B. Epel, and D. Goldfarb, *J. Magn. Reson.*, 2011, **208**, 95–102.
95. A. Giannoulis, C. L. Motion, M. Oranges, M. Bühl, G. M. Smith, and B. E. Bode, *Phys. Chem. Chem. Phys.*, 2018, **20**, 2151–2154.
96. A. Meyer, D. Abdullin, G. Schnakenburg, and O. Schiemann, *Phys. Chem. Chem. Phys.*, 2016, **18**, 9262–9271.
97. D. Abdullin, P. Brehm, N. Fleck, S. Spicher, S. Grimme, and O. Schiemann, *Chem. Eur. J*, 2019, **25**, 14388–14398.
98. R. Kappl, G. Bracic, and J. Hüttermann, in *High Resolution EPR*, eds. L. Berliner and G. Hanson, Springer New York, New York, NY, 2009, vol. 28, pp. 63–103.
99. N. Wili, S. Richert, B. Limburg, S. J. Clarke, H. L. Anderson, C. R. Timmel, and G. Jeschke, *Phys. Chem. Chem. Phys.*, 2019, **21**, 11676–11688.
100. D. Abdullin, *Appl Magn Reson*, 2020, **51**, 725–748.
101. A. Potapov, *J. Magn. Reson.*, 2020, **316**, 106769.
102. D. Abdullin, G. Hagelueken, R. I. Hunter, G. M. Smith, and O. Schiemann, *Mol. Phys.*, 2015, **113**, 544–560.
103. A. Marko and T. F. Prisner, *Phys. Chem. Chem. Phys.*, 2013, **15**, 619–627.